Systematic DFT+U and Quantum Monte Carlo Benchmark of Magnetic Two-Dimensional (2D) CrX$_3$ (X = I, Br, Cl, F)

Daniel Wines,

Materials Science and Engineering Division, National Institute of Standards and Technology (NIST), Gaithersburg, Maryland 20899, United States

Kamal Choudhary,

Materials Science and Engineering Division, National Institute of Standards and Technology (NIST), Gaithersburg, Maryland 20899, United States; Theiss Research, La Jolla, California 92037, United States

Francesca Tavazza

Materials Science and Engineering Division, National Institute of Standards and Technology (NIST), Gaithersburg, Maryland 20899, United States

Abstract

The search for two-dimensional (2D) magnetic materials has attracted a great deal of attention because of the experimental synthesis of 2D CrI$_3$, which has a measured Curie temperature of 45 K. Often times, these monolayers have a higher degree of electron correlation and require more sophisticated methods beyond density functional theory (DFT). Diffusion Monte Carlo (DMC) is a correlated electronic structure method that has been demonstrated to be successful for calculating the electronic and magnetic properties of a wide variety of 2D and bulk systems, since it has a weaker dependence on the Hubbard parameter (U) and density functional. In this study, we designed a workflow that combines DFT +U and DMC in order to treat 2D correlated magnetic systems. We chose monolayer CrX$_3$ (X = I, Br, Cl, F), with a stronger focus on CrI$_3$ and CrBr$_3$, as a case study due to the fact that they have been experimentally realized and have a finite critical temperature. With this DFT+U and DMC workflow and the analytical method of Torelli and Olsen, we estimated a maximum value of 43.56 K for the T_c of CrI$_3$ and 20.78 K for the T_c of CrBr$_3$, in addition to analyzing the spin densities and magnetic properties with DMC and DFT+U. We expect that running this workflow for a well-known material class will aid in the future discovery and characterization of lesser known and more complex correlated 2D magnetic materials.

Graphical Abstract

INTRODUCTION

Recently, the search for two-dimensional (2D) magnetic materials, especially ferromagnets, has become an important task for the materials science community. The revolutionary experimental synthesis of 2D CrI_3, which has a measured Curie temperature of 45 K,[1] has sparked interest in discovering and utilizing similar ferromagnetic materials for next generation devices. Beyond monolayer CrI_3, room temperature magnetism has been experimentally measured for 2D VSe_2 on a van der Waals substrate,[2] and it has been shown that ferromagnetic order exists in 2D $Cr_2Ge_2Te_6$[3] and Fe_3GeTe_2.[4] In addition, theoretical calculations have predicted ferromagnetic ordering in monolayers such as $CrBr_3$,[5] $CrCl_3$,[5,6] CrF_3,[7] MnO_2,[8,9] $FeCl_2$,[10] K_2CuF_4,[11] the family of MPX_3 (M is a 3d transition metal atom, X is a group VI atom),[12] a-$RuCl_3$,[13] $RuBr_3$, RuI_3,[14] and several other reported materials.[5]

Often times, however, these monolayers have a higher degree of electron correlation and require more sophisticated methods beyond density functional theory (DFT). Diffusion Monte Carlo (DMC)[15] is a many-body correlated electronic structure method that has been successful for the calculation of electronic and magnetic properties of a variety of bulk and low-dimensional systems.[16-40] This method has a much weaker dependence on the starting density functional and Hubbard parameter, can achieve results with an accuracy beyond DFT,[15] and scales similarly to DFT with respect to the number of electrons in the simulation.[15] For example, DMC has successfully predicted the magnetic structure for FeSe when DFT methods contradicted.[28] In addition, the correct spin superexchange in the correlated cuprate Ca_2CuO_3 has been determined[27] using DMC methods.[27] With regards to 2D materials and DMC, the band gap of GaSe[31] has been calculated to be in excellent agreement with experiment, the correct atomic structure and potential energy surface of CrI_3[39] and GeSe[30] have been predicted, and the critical temperature of MnO_2[9] has been estimated.

The last step in the investigation of 2D correlated magnetic systems is the estimation of T_c. Specifically, the Mermin-Wagner theorem[41] implies that magnetic order in a monolayer

cannot exist unless magnetic anisotropy (MA) is present and perpendicular to the plane, which allows a finite critical temperature (T_c). In order to obtain an appropriate value for T_c, the magnetic anisotropy energies (MAE) should be determined by performing noncollinear (spin–orbit) calculations. Once the MAE and magnetic exchange parameters of a 2D system are obtained from first-principles, they can be input into analytical models such as the one derived by Torelli and Olsen[42] to estimate T_c.

Data-driven high-throughput studies of 2D materials are needed to identify candidates that meet the criteria to be a 2D ferromagnet with a finite T_c. Development of an efficient framework dealing with all the computational steps highlighted above is necessary to make such a high-throughput search possible.

In this work, we developed one such workflow and used it to perform a systematic DFT+U and Quantum Monte Carlo benchmark of magnetic two-dimensional (2D) materials. The framework and data it produced have been made available to the public through the JARVIS (Joint Automated Repository for Various Integrated Simulations, https:// jarvis.nist.gov/) project. JARVIS, which is part of Materials Genome Initiative (MGI), is a computational materials science framework developed at National Institute of Standards and Technology (NIST).[43] One of the main components, JARVIS-DFT, is a comprehensive database of DFT-computed material properties for over 3000 2D and 2D-like materials and over 60 000 bulk materials, with results from multiple functionals such as PBE and vdW-DF-OptB88. JARVIS-DFT contains DFT-calculated structural, energetic,[44] elastic,[45] optoelectronic,[45] thermo-electric,[46] piezoelectric, dielectric, infrared,[47] solar-efficiency,[48] topological,[49] anomalous quantum confinement,[50] and superconducting[51] properties. As a response to the limitations of DFT, a limited number of beyond-DFT data, such as hybrid functionals (HSE06, PBE0) or many-body (GW, DMFT) results have been added to JARVIS, to increase accuracy and reliability of data. The discrepancies observed in DFT results, between different density functionals and experimental data, are more prevalent for materials that have a higher degree of electron correlation and are common for the 2D magnetic structures of interest. Specifically, this failure of DFT to describe correlated systems can be due in part to the tendency of standard exchange-correlation functionals to overdelocalize valence electrons.[52] That is why DFT fails for systems whose ground state is characterized by a more pronounced localization of electrons, such as transition-metal-based materials. This delocalization occurs due to the inability of the exchange-correlation functional to completely cancel out the electronic self-interaction, and a fragment of the same electron remains that can induce added self-interaction, inducing an excessive delocalization of the wavefunction.[52] To combat this self-interaction error, more sophisticated density functionals such as meta-GGAs,[53,54] hybrid functionals,[55] or DFT functionals with the added Hubbard (U) correction[56] can be utilized. Despite the fact that these more sophisticated DFT methods exist, often times, the calculated properties of 2D magnets are heavily influenced by which density functional and U parameter are used. Due to this, a method that has a weaker dependence on the U parameter and functional and can capture the electron correlation that drives magnetic ordering is required. With such a many-body method, the realization of a 2D magnetic device fabrication can be significantly expedited.

The goal of this study is to utilize a higher-order many-body method such as DMC, in order to treat 2D correlated magnetic systems. We chose monolayer CrX_3 (X = I, Br, Cl, F) as a case study because they are an ideal class of materials to benchmark, due to the fact that they have been experimentally realized,[1,57,58] have a finite critical temperature,[1,5] and have extensively been studied with DFT.[5] We hope that making such a DMC framework public through the JARVIS project, for a well-known class of materials, will aid in the future discovery and characterization of lesser known and more complex correlated 2D materials.

The outline of this paper is as follows: The Computational Methods section will outline the computational approaches for DFT, Quantum Monte Carlo (QMC), and postprocessing of QMC data as well as detail the newly developed DFT-QMC JARVIS workflow to obtain accurate magnetic properties of 2D systems. The Results and Discussion section will present DFT benchmarking using various DFT methods and QMC results, and the Conclusion section will provide concluding remarks.

COMPUTATIONAL METHODS

DFT and QMC Methods.

We performed DFT calculations with the added Hubbard correction (U)[56] to treat the on-site Coulomb interaction of the $3d$ orbitals of Cr atoms. To determine how the choice of functional impacts the results, benchmarking DFT simulations were performed using the Vienna Ab initio Simulation (VASP) code and projector augmented wave (PAW) pseudopotentials[59,60] (please note that the use of commercial software (VASP) does not imply recommendation by the National Institute of Standards and Technology). It is advantageous to benchmark these materials with VASP and PAW pseudopotentials due to the fact that they require a much smaller cutoff energy and are therefore more cost-effective for a large number of simulations. For these reference calculations, the Perdew–Burke–Ernzerhof (PBE),[61] local density approximation (LDA),[62] the strongly constrained and appropriately normed (SCAN),[53] meta-GGA, and recently developed r2SCAN[54] functionals were used. r2SCAN was developed to improve the numerical performance of SCAN, at the expense of breaking constraints known from the exact exchangecorrelation functional.[54] In addition, to increase accuracy, we also performed calculations with the screened hybrid HSE06 functional, which is created by mixing 75% of the PBE exchange with 25% of the Fock exchange and 100% of the correlation energy from PBE.[55] For our VASP calculations using PBE, LDA, SCAN, and r2SCAN (+U), we used the Cr_{pv} PAW potential (12 electrons), while for HSE06, we used the standard Cr PAW potential (6 electrons) due to computational restraints. We justified this choice for the HSE06 calculations by performing PBE+U ($U = 2$ eV) calculations with the Cr_{pv} PAW potential and the Cr standard PAW potential separately, and found the results for magnetic exchange to be within 2–4% of each other. There was at least 20 Å space of vacuum given between periodic layers of CrX_3 in the c-direction. We used a kinetic energy cutoff of 500 eV for CrI_3, $CrBr_3$, and $CrCl_3$ and a cutoff of 700 eV for CrF_3. A $5 \times 5 \times 1$ k-point grid was used for the eight atom unit cell of all CrX_3 monolayers. To calculate MAE, spin–orbit DFT (DFT+U) calculations were carried out for the FM and AFM states of each 2D CrX_3. This is done by performing two spin–orbit calculations, one where the spins are oriented in the off-plane direction (in our case, z) and one where the

easy axis is rotated $90°$ (in our case, *x*). A workflow where these four static spin–orbit calculations (for the FM and AFM phases) are performed (using the previously optimized vdW-DF-OptB88[63] geometry) was carried out within JARVIS.

For all QMC calculations, we used DFT and the PBE functional to create the trial wave function for subsequent fixed-node DMC calculations. The Quantum Espresso (QE)[64] code was used for the DFT calculations within our QMC workflow. The trial wave function was generated separately for the FM and AFM configurations of each CrX_3 monolayer, using various values of *U*. The reason for this was to variationally determine the optimal nodal surface (find the value of *U* that produces the lowest total energy). All QMC calculations require norm-conserving (NC) pseudopotentials. For Cr, we used hard NC RRKJ (OPT), scalar relativistic pseudopotentials.[65] For Br, Cl, and F, scalar relativistic effective core potentials (ECP) were used.[66,67] For I, a newly developed averaged relativistic effective potential (AREP) was used.[68] For DMC calculations that explicitly include spin–orbit effects, a spin–orbit relativistic effective potential (SOREP) for I[68] could be used, but since the spin–orbit interaction of CrI_3 is on the order of the DMC error bar, we decided to use the AREP potential for I. These NC potentials are meant to produce all electron results (in accordance with coupled cluster theory), while the PAW pseudopotentials are meant to reproduce all electron density functional results. Ideally, the energy differences obtained with either method should yield similar results, which we verify by observing a 2–6% difference between PAW results and NC results for magnetic exchange (for PBE+U, $U = 2$ eV). For these pseudopotentials, we used a kinetic energy cutoff of 300 Ry (~4080 eV) for all calculations, with the exception of F, which required 600 Ry (~8160 eV, see Figure S1). We tested the reciprocal grid size at the DFT level and determined that a k-grid of $3 \times 3 \times 1$ was sufficient for each CrX_3 monolayer (see Figure S2). Although three different types of pseudopotentials were used in our calculations (PAW for DFT benchmarking, PAW_{pv} for HSE06 benchmarking, and NC for DMC), the results at the DFT level are all within 2–8% of each other, which indicates that pseudopotential choice does not significantly hinder the accuracy of such small energy scale calculations.

The QMCPACK[69,70] code was used to carry out variational Monte Carlo (VMC) and DMC[15,71] calculations, after the DFT generation of the trial wave function. VMC calculations are the intermediate steps between the DFT and DMC calculations, where the single determinant wave function from DFT is converted into a many-body wave function by use of the Jastrow parameters,[72,73] which aid in modeling the electron correlation and ultimately reduce the uncertainty in the DMC simulations.[74,75] Up to two-body Jastrow[76] correlation functions were included in the trial wave function. The linear method[77] was used to minimize the variance and energy respectively of the VMC energies. The cost function of the variance optimization is 100% variance minimization, while the cost function of the energy optimization is split as 95% energy minimization and 5% variance minimization, which has been demonstrated to reduce the uncertainty for DMC results.[74] The DFT-VMC-DMC workflows were automated using the Nexus[78] software suite. After testing, a large supercell size of 48 atoms was deemed to be sufficient in eliminating finite-size effects for the FM and AFM configurations of 2D CrI_3 (see Figure S3), which justified our choice to use a 48 atom supercell to calculate the magnetic exchange energy with QMC for the other materials of interest. For the DMC simulations, the T-moves[79] algorithm was used

to evaluate the nonlocal part of the pseudopotentials, and after testing, a time step of 0.01 Ha^{1-} was determined to be sufficient (see Table S1). The error in our DMC calculations is the standard error about the mean value. This ±value about the mean is indicated by the error bars in the figures and the parentheses in the tabulated results. As previously stated, in our DMC simulations, controllable errors such as time step, finite size, and choice of nodal surface are appropriately addressed. The remaining sources of uncertainty can arise from the fixed-node bias and the error associated with evaluating the nonlocal part of the pseudopotential. Luckily, the fixed-node error has been demonstrated to be on the order of 1–2% in other crystal systems,[26] and the T-moves[79] algorithm has been proved to be successful in evaluating the nonlocal part of the pseudopotential, since it is treated in a variational way.[26,79]

The total charge and spin densities were extracted from our DMC results. The spin density (ρ_s) is the difference between the spin-up contribution to the total charge density and the spin-down contribution to the total charge density ($\rho_s = \rho_{up} - \rho_{down}$). We used an extrapolation scheme on the DMC densities in order to eliminate the bias that occurs from using a mixed estimator. Because the density estimator does not commute with the fixed-node Hamiltonian, the DMC density we calculated is a mixed estimator between the pure fixed-node DMC and VMC densities. The extrapolation formula takes the form:[15]

$$\rho_1 = 2\rho_{DMC} - \rho_{VMC} + \mathcal{O}\left[(\Phi - \Psi_T)^2\right] \tag{1}$$

where ρ_{DMC} and ρ_{VMC} are the DMC and VMC charge densities, respectively. Φ is the trial wave function arising from the DMC Hamiltonian, and Ψ_T is the trial wave function arising from VMC.

We integrated the DFT (DFT+U) and DMC spin densities up to a cutoff radius r_{cut} (which is defined as half of the Cr—X bond distance in CrX_3 monolayers) to obtain an estimate for the site-averaged atomic magnetic moment per atom. To calculate these magnetic moments per atom (M_A), we summed over the spherically interpolated spin densities:

$$M_A = 4\pi \int_0^{r_{cut}} r^2 \rho_s(r) \mathrm{d}r \approx 4\pi \sum_{i=0}^{r_{cut}/\Delta r} r_i^2 \rho_s(r_i)\Delta r \tag{2}$$

where r is the radial grid size and r_i is the distance from the center of the atom to a given point on the grid.

To estimate the critical temperature of CrX_3 monolayers, we used the method outlined by Torelli and Olsen,[42] which derived a simple expression for T_c of 2D ferromagnets by fitting classical Monte Carlo results for different lattice types. The expression they derived is a solely a function of the first-principles obtained MAE and magnetic exchange constants. By calculating the magnetic exchange constants with DMC and the MAE from DFT+U, we were able to obtain an estimate of T_c for the monolayers.

JARVIS Workflow.

The full form of the 2D model spin Hamiltonian[42,80] takes the form:

$$\mathscr{H} = -\left(\sum_i D(S_i^z)^2 + \frac{J}{2}\sum_{i,i'}\vec{S}_i \cdot \vec{S}_{i'} + \frac{\lambda}{2}\sum_{i,i'}S_i^z S_{i'}^z\right) \tag{3}$$

where the sum over i runs over the lattice of Cr atoms and i' runs over the nearest Cr site of atom i due to a strong magnetic moment localized on Cr atoms. Due to the fact that long-range interactions have previously been shown to die out in 2D CrI$_3$,[80] we focused solely on the nearest neighbor interactions (our calculations consisted of a unit cell of two Cr atoms and six X atoms). From this unit cell (which is depicted in Figure 1), we adopt two magnetic orientations: ferromagnetic (FM), consisting of two spin-up Cr atoms, and antiferromagnetic (AFM), consisting of one spin-up Cr atom and one spin-down Cr atom. This nearest neighbor AFM magnetic configuration is commonly referred to as the Neel configuration.[80]

The first term in the spin Hamiltonian refers to the easy axis single ion anisotropy (z chosen as the off-plane direction). The second term describes the Heisenberg isotropic exchange, and the last term describes the anisotropic exchange. The sign convention is as follows: $J > 0$ favors FM interactions, $D > 0$ favors off-plane easy axis, and $\lambda = 0$ implies full isotropic exchange. We treat eq 3 classically, describing the spins $\vec{S}$ collinearly as either $S = S^x$ or $S = S^z$. By doing this, it possible to write the energy of the four possible magnetic ground states: (i) ferromagnetic off-plane (FM, z), (ii) antiferromagnetic off-plane (AFM, z), (iii) ferromagnetic in-plane (FM, x), and (iv) antiferromagnetic in-plane (AFM, x). The corresponding energy equations take the form:

$$E_{\text{FM},z} = -2S^2 D - 3S^2(J+\lambda) \tag{4}$$

$$E_{\text{AFM},z} = -2S^2 D + 3S^2(J+\lambda) \tag{5}$$

$$E_{\text{FM},x} = -3S^2 J \tag{6}$$

$$E_{\text{AFM},x} = +3S^2 J \tag{7}$$

where $S = 3/2$. This model has been extensively used to model 2D magnetism.[5,80] However, the model assumes diagonal exchange interaction and does not include Dzyaloshinskii-Moriya interactions, Kitaev interactions, or higher-order spin interactions. Recently, there have been attempts to modify this model with various types of spin interactions, but presently, the roles of the different terms are not completely understood. Most importantly, there are strong disagreements between calculations[81,82] and experiments[83] in regards to the magnitude of Kitaev interactions.

To obtain initial reference values for J, λ, and D, we performed self-consistent noncollinear DFT calculations in VASP (PAW). In these spin–orbit calculations, we rotated the easy axis by 90° and calculated the energy difference between the rotated and nonrotated

configurations separately for FM and AFM. Since the magnetic anisotropy calculations are more difficult to converge than the total energy, we adjusted certain parameters to allow for careful convergence. Specifically, the cutoff energy was increased by 100–200 eV, the electronic convergence threshold was decreased to 1.0×10^{-7} eV, symmetry was turned off, and the well-converged k-point grid obtained from JARVIS was used.[84] Upon comparison to the magnetic anisotropy energy results from other recent studies[5,10,42] that used even higher convergence criteria (cutoff energy, k-points, supercell size), our results are in excellent agreement, which further demonstrates that our results are carefully converged. These four DFT calculations were automated using the JARVIS workflow, where four distinct total energy values were calculated for each material. This workflow was benchmarked for 2D CrI_3 (JVASP-76195), $CrBr_3$ (JVASP-6088), $CrCl_3$ (JVASP-76498), and CrF_3 (JVASP-153105) for using multiple flavors of DFT (discussed in detail in DFT Benchmarking section).

Although performing these four noncollinear DFT+U calculations is a robust method for determining the magnetic exchange and anisotropy parameters of a 2D system, these results can be systematically improved with QMC simulations. QMC can improve the magnetic property predictions in two ways. First, one can variationally determine the optimal U value using DMC (discussed in further detail in the following section), and second, a statistical bound can be calculated for the J parameter by performing DMC simulations for the FM and AFM phases separately. It is important to note that these QMC energies are collinear (spin-polarized), in contrast to the previous noncollinear (spin–orbit) DFT calculations. Currently, spin–orbit implementation is limited in DMC. For this reason, we neglect the λ contribution when calculating J with QMC using eqs 4 and 5, since such a contribution can only be obtained from spin–orbit calculations. This does not have a significant impact the final result for J, since $J \gg \lambda$. As a result, we design a high-throughput workflow that allows us to variationally determine the optimal value of U using DMC, calculate a statistical bound on J by performing collinear DMC calculations for the FM and AFM phases, and use that optimal determined U to perform DFT+U simulations and extract the anisotropy parameters (D, λ), with the end goal of using these parameters to accurately estimate the 2D critical temperature. A full schematic of this workflow is depicted in Figure 2.

It is possible to estimate the critical temperature using the analytical method outlined in Torelli and Olsen[42] with our obtained values of J, D, and λ. In Torelli's work, classical Monte Carlo and random phase approximation (RPA) simulations were used to derive a simple expression for T_c that depends solely on lattice type and the ab initio exchange coupling constants. The analytical function for T_c takes the form:

$$T_c = T_c^{\text{Ising}} f(x) \tag{8}$$

with

$$f(x) = \tanh^{1/4}\left[\frac{6}{N_{\text{nn}}}\log(1 + \gamma x)\right] \tag{9}$$

where N_{nn} is the number of nearest neighbors and $\gamma = 0.033$ (dimensionless constant). T_c^{Ising} is the critical temperature for the standard Ising model, which can be written as $T_c^{\text{Ising}} = S^2 J \tilde{T}_c / k_B$ where $\tilde{T}_c$ is the fitted dimensionless critical temperature (1.52 for a honeycomb lattice). In cases where single ion anisotropy and anisotropic exchange are present, $x = \Delta / J(2S - 1)$, where Δ is the spin gap:

$$\Delta = D(2S - 1) + \lambda S N_{nn} \tag{10}$$

Postprocessing of the energies to determine J, D, λ, and, finally, T_c were also carried out within the JARVIS workflow.

RESULTS AND DISCUSSION

DFT Benchmarking.

Prior to incorporating QMC calculations in the workflow (as depicted in Figure 2), we performed reference DFT calculations using VASP (PAW) to benchmark the magnetic properties of monolayer CrX_3 (X = I, Br, Cl, F). Performing these reference calculations in VASP is advantageous because it allows us to perform spin–orbit calculations, and the DFT calculations come at a much lower cost than those performed with the NC pseudopotentials in QE (due to higher cutoff energy). Due to these advantages, we performed these calculations with a variety of local and semilocal density functionals such as PBE, LDA, SCAN, r2SCAN (with and without a U correction of 2 eV), and HSE06, including spin–orbit effects, to identify if such a choice made a real difference. Table 1 depicts the values of J, D, λ, and T_c calculated with each functional, using static geometry (depicted in Figure 1) and structures taken from the JARVIS-DFT database, where the geometry was optimized with vdW-DF-OptB88. A scatter plot of the data presented in Table 1 is depicted in Figure S4. The reason we did not perform this workflow with vdW-DF-OptB88 is because spin–orbit coupling is not compatible with vdW functionals such as vdW-DF-OptB88.[63] Similar to previous DFT results, CrI_3 has the highest degree of MA when compared to the other 2D CrX_3 materials. This is due to the larger contribution of spin–orbit coupling that can be attributed to the I atoms in the cell. Depending on functional, a wide variety of J is predicted for CrI_3, ranging from 1.98 to 4.22 meV. This drastic difference in magnetic exchange demonstrates the shortcomings of local/semilocal density functionals being used to deal with correlated electronic systems. This wide, functional-dependent spread in J is also observed for 2D $CrBr_3$, $CrCl_3$, and CrF_3 (see Table 1). Since the magnetic exchange is the driving force behind the magnitude of the Curie temperature, the estimation of J is crucial for an accurate T_c. For example, the LDA J value of 1.98 yields a T_c of 27.09 K, and the HSE06 J value yields a T_c of 48.63 K for CrI_3. With respect to the experimental value of $T_c = 45$ K for CrI_3,[1] PBE+U, SCAN+U, and HSE06 are closest.

In terms of the MA of CrI_3 (D and λ), there is a relatively consistent trend between density functionals, with the exception of SCAN and SCAN+U. For SCAN and SCAN +U, the in-plane easy axis is favored ($D < 0$) and for pure SCAN, a smaller value of λ combined with this negative D results in a negative spin gap (see eq 10) and a nonphysical critical

temperature in the Torelli and Olsen model. This negative spin gap behavior as a result of SCAN is not unique to CrI_3. As seen in Table 1, this occurs for $CrBr_3$ (calculated with SCAN+U) and CrF_3 (calculated with SCAN). This behavior can be due in part to the numerical instabilities of the SCAN functional when being used to calculate properties of complex and correlated systems. This is even more evident when comparing SCAN and SCAN+U findings to r2SCAN and r2SCAN+U (r2SCAN is meant to correct the numerical instabilities in SCAN[54]) results, where we only obtain positive spin gaps and finite T_c (see Table 1). In recent literature, concerns about the performance of the SCAN functional for magnetic materials have been brought up, including the overmagnetization of transition metal solids, deeming SCAN inappropriate for open shell metallic ferromagnetic metals.[85,86] However, SCAN has been reported to yield accurate properties across all bulk MnO_2 polymorphs.[87] Regardless of these successes and concerns, we believe it is important to report these SCAN results as a benchmark to compare DMC and other density functionals to.

In addition to performing this DFT/DFT+U workflow for a fixed geometry, we investigated the geometry dependence on the magnetic exchange and anisotropy. We did so by first relaxing the FM orientation of each structure with each respective functional (PBE, LDA, SCAN, r2SCAN, and +U for each) using spin-polarized DFT (as opposed to spin–orbit DFT, which comes at a much higher computational cost for geometric relaxation calculations). The relaxation using HSE06 was omitted due to the high computational expense of such calculations. Once the relaxed FM geometry was obtained, we fixed this geometry and performed the same noncollinear DFT (as Table 1) workflow to obtain the magnetic constants. The results of these calculations are presented in Table 2, and the relaxed structural parameters are given in Table S2. A scatter plot of the data presented in Table 2 is depicted in Figure S5.

For the most part, geometry has little effect on the magnetic properties of each monolayer, which implies that the functional dependence is stronger. When comparing Tables 1 and 2 for 2D CrI_3, we observe that the J parameters and T_c values are consistent between whether the geometry is relaxed or the geometry is fixed to the vdW-DF-OptB88 (JARVIS) structure. The only exception of this is the LDA relaxed geometry, where the lattice parameters are severely underestimated (see Table S2) for CrI_3, and subsequently, the values for J and T_c are much lower than expected (1.13 meV and 17.16 K). This LDA trend also occurs for monolayer $CrBr_3$, $CrCl_3$, and CrF_3. For $CrCl_3$, the lattice compression from the LDA relaxation causes a magnetic phase transition from FM favorable to AFM favorable (see negative J value in Table 2). This compression-induced phase transition has been reported theoretically for 2D $CrCl_3$ in Dupont et al.[6] Changes in the MA energy with respect to geometry are most prevalent for 2D $CrCl_3$, where we see a shift from out-of-plane easy axis (D > 0) to in-plane easy axis (D < 0) favorability for PBE and r2SCAN. This sign change in D occurs while relaxing with the respective functionals for $CrCl_3$, but there is only a small shift in T_c (between Tables 1 and 2) due to the fact that J is the driving force behind the critical temperature. For these reasons, we proceeded to use the vdW-DF-OptB88 relaxed geometry for subsequent QMC calculations in the next section. Further justification of using the vdW-DF-OptB88 geometry for QMC calculations stems from the fact that the geometry of 2D CrI_3 calculated with vdW-DF-OptB88 is in identical statistical agreement with the

geometry calculated from a previous DMC study from Staros et al.[39] (see Table S2). In addition, the lattice constant obtained with vdW-DF-OptB88 for 2D $CrCl_3$ is in the closest agreement with the bulk lattice constant of layered $CrCl_3$[88] (see also Table S2).

Although the structural parameters impact the magnetic properties of $CrCl_3$ more significantly than CrI_3, $CrBr_3$, and CrF_3 (see difference between Table 1 and Table 2), overall the functional dependence is stronger than the structural dependence. For comparison purposes, we present literature results[5,7,42,80,82,89-92] for all four monolayers calculated with a variety of computational methods in Table S3. Similar to our own results, we see a large variability in J and T_c with respect to the computational method used, but we observe the same overall trends between each material. This is especially prevalent in works such as the one by Pizzochero et al.,[92] which benchmarks the properties of CrI_3 for a variety of DFT methods and multireference configuration interaction (MRCI) theory.

This high-throughput benchmarking with VASP is an important preliminary step in identifying the key areas where higher-order correlated methods such as QMC can be used to improve electronic and magnetic property prediction. The next section will detail the process of incorporating QMC calculations into the workflow (as depicted in Figure 2) and provide a deeper analysis of our QMC results.

QMC Results.

QMC calculations in this study (which consist of a VMC calculation to optimize the Jastrow parameters of the wave function, followed by a DMC calculation) require a well-converged trial wave function that is created via a DFT calculation. As opposed to the VASP DFT (PAW) calculations in the previous section, the DFT calculations detailed in this section (for additional benchmarking and creating the trial wave function) are performed using NC pseudopotentials (for additional information, see Computational Methods). DMC has the property of zero-variance, which means that as the trial wave function approaches the exact ground state (exact nodal surface), the statistical fluctuations in the energy reduce to zero.[15] There have been reported instances where various sophisticated and expensive methods have been used to optimize the nodal surface of the trial wave function.[93-96] Similar to other DMC studies of magnetic materials,[9,19,27,29,39,97] we employed a PBE +U approach where the Hubbard U value was used as a variational parameter to optimize the nodal surface using DMC. Since we can determine the optimal U parameter variationally using DMC, it makes our final results more reliable than solely using DFT+U, where the U parameter is arbitrarily chosen or fitted to experimental data. In addition, the DMC determined U value can be used for subsequent DFT +U calculations, giving a more reliable and less costly method to compute correlated material properties.

Figure 3 depicts the total energies of a 16 atom supercell (normalized per formula unit (f.u.)) of the FM orientation of 2D (a) CrI_3 and (b) $CrBr_3$, while Figure S6 depicts (a) $CrCl_3$ and (b) CrF_3 calculated as a function of the U parameter, with the goal of variationally determining the optimal trial wave function. For convenience of presentation, the DMC energies are shifted by the lowest DMC energy obtained at the appropriate U value ($U = 2$ eV for CrI_3 and $CrBr_3$, $U = 1$ eV for $CrCl_3$, and $U = 4$ eV for CrF_3). Unsurprisingly, the U value that yields the lowest energy for 2D CrI_3 is 2 eV, which is similar to the result obtained

by Staros et al.[39] $U = 2$ eV also yields the lowest energy for CrBr$_3$, but the difference in energy between $U = 2$ eV, and other values of U are much larger than that of CrI$_3$, indicating that the U dependence on the trial wave function is stronger for 2D CrBr$_3$. As seen in Figure S6a,b, $U = 1$ eV produces an optimal wave function for CrCl$_3$ and $U = 4$ eV produces an optimal wave function for CrF$_3$. Although these U values differ from the $U = 2$ eV value for CrI$_3$ and CrBr$_3$, the energies at the minimum points are statistically identical to the energy produced at $U = 2$ eV for CrCl$_3$ and CrF3.

Due to the fact that 2D CrI$_3$ and CrBr$_3$ have the highest predicted T_c out of the four CrX$_3$ monolayers (at the DFT level, see Tables 1 and 2) and the fact that the largest discrepancy in predicted J and T_c occurs for CrI$_3$ and CrBr$_3$, we decided to focus primarily on these two materials for the remainder of this study. Therefore, we ran monolayer CrI$_3$ and CrBr$_3$ through the full workflow depicted in Figure 2, with the goal of determining a statistical bound on J and T_c. In order to compute J, we had to perform calculations for both monolayers in the FM and AFM (Neel) configurations. We performed these calculations using NC pseudopotentials (as previously mentioned) and based on our results presented in Figure 3a,b, created the trial wave function with PBE+U ($U = 2$ eV). For the sake of completeness, we also determined that $U = 2$ eV yields the optimal wave function for the AFM phase of CrI$_3$ and CrBr$_3$ (see Figure S7), and this was used for all subsequent DMC calculations of the AFM phase. In addition, we performed these QMC simulations at a supercell size of 48 atoms (see Figure S3 for convergence details). Figure 4 depicts the calculated J parameter of 2D (a) CrI$_3$ and (b) CrBr$_3$ using PBE+U (red triangle) and DMC (blue square). It is important to note that the DMC simulations required to achieve an estimate for J (both FM and AFM calculations) require significant computational resources. Specifically, the DMC estimate of J required ~1.0×10^6 seconds/node to properly reduce the uncertainty (further details in the Supporting Information). With more substantial computational resources beyond our capabilities, the uncertainty could be further reduced. As expected with PBE+U, as the U value increases from $U = 0$ to 4 eV, the J parameter also increases linearly. In comparison to the PBE+U values, the average DMC-calculated J for CrI$_3$ falls slightly under that of the PBE+2 value, with the error bar overlapping with the DFT values at $U = [0, 1, 2]$ eV. For 2D CrBr$_3$, the average value of J falls about 1 meV under the PBE+2 value, with the error bar overlapping with the DFT values at $U = 0$ and 1 eV. We report a DMC J value of 2.49(1.16) meV for 2D CrI$_3$ and a value of 1.30(1.00) meV for 2D CrBr$_3$. This average DMC value of 2.49(1.16) meV for CrI$_3$ is in excellent agreement with the MRCI-calculated value of 2.88 meV reported in Pizzochero et al.[92] (see Table S3).

In order to understand the implications of the DMC results presented in Figure 4, we went a step further and calculated the Ising temperature (as described in the JARVIS Workflow section) and Curie temperature (T_c, calculated with the Torelli and Olsen model). These results are presented in Table 3. It is important to reiterate that the PBE+U and DMC J (and subsequent T_c^{Ising}) values are determined from spin-polarized calculations and NC pseudopotentials, while the MA that is used in the Torelli and Olsen model to determine T_c is carried out using VASP with PAW pseudopotentials (from the DFT Benchmarking section). This combination of methods (out-lined in Figure 2) allows us to put a statistical bound on T_c for a given magnetic material. As seen in Table 3, we present T_c calculated

with various values of J (rows: PBE+U with varying U and DMC at $U = 2$ eV) and various values for the MA parameters (columns: using various functionals at the optimal U of 2 eV, indicated by the superscript on T_c). It is clear from Table 3 that J is more of a driving force behind the variability of T_c than the MA. The largest difference in anisotropy (and therefore T_c) occurs for r2SCAN+2 for CrI$_3$ and r2SCAN+2 and HSE06 for CrBr$_3$, with respect to other functionals used to calculate anisotropy. Similarly to the data reported in Table 1, we observe a nonphysical T_c for CrBr$_3$ with MA calculated with SCAN+2 (due to a negative spin gap). For 2D CrI$_3$, we obtain a statistical bound of $T_c = 43.56$ K using the J obtained from DMC and the anisotropy parameters obtained from HSE06, which is in excellent agreement with the measured value of 45 K.[1] For 2D CrBr$_3$, we obtain a maximum value of $T_c = 20.78$ K using the J obtained from DMC and the anisotropy parameters obtained from LDA+2. For the sake of completeness, we calculated the T_c with a fixed J obtained from DMC and the anisotropy (D and λ) from a wider range DFT functionals, resulting in a sweep of possible values for T_c (a more detailed extension of Table 3). This thorough sensitivity analysis of the DMC-DFT-calculated critical temperature is given in Table S4, where we observe that the different values of anisotropy have a ~20% impact on the variability of the critical temperature for CrI$_3$ and CrBr$_3$. Interestingly, anisotropy obtained from PBE (no U correction) results in a slightly higher critical temperature for both monolayers (and bare LDA for CrBr3), but we find our maximum value estimates of $T_c = 43.56$ K and $T_c = 20.78$ K (for CrI$_3$ and CrBr$_3$ respectively) to be more reliable, since the anisotropy was obtained from hybrid and Hubbard corrected functionals. Although these critical temperatures are far below room temperature, it has been demonstrated that T_c can be increased by applying strain[8] or by changing the monolayer substrate.[2]

As an additional benchmark, we extracted the total charge density from our DMC simulations of 2D CrI$_3$ and CrBr$_3$ (using a trial wave function at $U = 2$ eV and a 48 atom supercell). From the total charge densities, we were able to determine the spin densities ($\rho_{up} - \rho_{down}$), which are depicted in the insets of Figure 5a,c for CrI$_3$ and CrBr$_3$ respectively. From this many-electron DMC approach, we observe that for both materials, the Cr atoms are highly spin-polarized, while the I and Br atoms are slightly polarized antiparallel with respect to the Cr atoms. We went a step further by plotting the radial averaged densities as a function of distance for Cr and I separately for CrI$_3$ and Cr and Br separately for CrBr$_3$. This gives us the spatial variations in total charge density (Figure S8) and spin density (Figure 5). We benchmarked these radially averaged densities with PBE+U ($U = [0, 1, 2, 3, 4]$ eV) using NC pseudopotentials in QE.

Figure S8a,c depicts the radially averaged total charge density of the Cr atoms as a function of distance for CrI$_3$ and CrBr$_3$ respectively. We observe that while the PBE+U results are almost identical for the Cr atoms for both materials, the total charge density of Cr is overestimated (mostly around the peak) with respect to the DMC total density. Although this PBE+U overestimation occurs for both CrI$_3$ and CrBr$_3$, it is much more apparent for CrBr$_3$ (see Figure S8c). For I and Br (Figure S8b,d)), the difference between the PBE+U and DMC total charge density is negligible. The larger discrepancy between DMC and PBE+U for the Cr atom (for both CrI$_3$ and CrBr$_3$) near the radial density peak (peak of d orbital) is due in part to the fact that DFT functionals tend to unsuccessfully capture 3d orbitals. Although this sizable difference between PBE+U and DMC occurs for the total charge densities, it has

been reported that various DFT methods can give a more accurate description of the spin density than the total charge density.[38] Figure 5 depicts the radially averaged spin densities for each atom of 2D CrI_3 and $CrBr_3$. For CrI_3 (Figure 5a,b), we observe excellent agreement between the DMC and PBE+2 spin densities for Cr and I, indicating that the PBE+2 method does not only reproduce a correct T_c with respect to DMC but also correct spin density. In contrast, the results for $CrBr_3$ are slightly different. Although it was determined that PBE+2 yields the most optimal wave function for DMC (Figure 3b), the DMC spin density of Cr in $CrBr_3$ is closest to the PBE+0 result (see Figure 5c). This is consistent with the trend of the DMC-calculated J (and T_c) overlapping more closely with PBE +0 for $CrBr_3$ (see Figure 4b and Table 3). As for the Br atom in $CrBr_3$, the DMC spin density is within the margin of error of that calculated with PBE+U for $U = [0, 1, 2,$ and $3]$ eV. Most importantly for both materials (Figure 5b,d), the antiparallel polarization of I and Br with respect to Cr is present for DMC and all PBE+U results.

We went one step further and estimated the site-averaged atomic magnetic moments per Cr and I for 2D CrI_3 and Cr and Br for $CrBr_3$ by integrating the spin densities depicted in Figure 5. These tabulated magnetic moments are presented in Table 4. The results of Table 4 are consistent with the spin density results presented in Figure 5, where we see that the DMC-calculated magnetic moment for CrI_3 is closest to PBE +2, and the DMC-calculated magnetic moment of $CrBr_3$ is closest to PBE+0. Since PBE+0 produces results closest to DMC, we decided to recalculate the T_c using the anisotropy from PBE+U ($U = 0$ eV). We find that this increases the DMC maximum value to $T_c = 21.39$ K, which is about 1 K larger than previously reported (see Table S4). By analyzing and integrating the spin densities, we obtain a clear picture of how the magnetization of each ion depends on the computational method used. These results serve as a many-body theoretical benchmark for the magnetic properties of 2D CrI_3 and $CrBr_3$ and give information on how to assess the accuracy of DFT calculations with various Hubbard corrections.

CONCLUSION

In this work, we designed and applied a workflow that combines DFT+U, QMC (VMC, DMC), and analytical models to estimate a statistical bound for the critical temperature of a 2D magnetic system. Such a workflow is intended to be integrated into the JARVIS framework. We chose monolayer CrX_3 (X = I, Br, Cl, F) as a case study, since they have been experimentally realized and have a finite critical temperature. After extensive DFT+U benchmarking with several functionals, we deemed that 2D CrI_3 and $CrBr_3$ were worthwhile to run through the more computationally expensive DFT+U and QMC workflow, due to their higher T_c and higher degree of disagreement between DFT functionals. After variationally determining the optimal wave function for DMC (Hubbard U value used in the DFT wave function generation), we calculated a maximum value of 43.56 K for the T_c of CrI_3 and of 20.78 K for the T_c of $CrBr_3$. We also extracted the spin density from our DMC results for Cr and I atoms separately for CrI_3 and Cr and Br atoms separately for $CrBr_3$ and provide a detailed comparison with DFT+U. In terms of the workflow, this procedure can be used for the investigation of future 2D magnetic systems that have a higher degree of complexity and electron correlation, such as transition metal oxides. The findings of this specific case study show the successes of the DMC method when applied to a 2D magnetic system and provide

a many-body theoretical benchmark for CrX_3 monolayers that will guide experimentalists in characterizing 2D magnets.

Supplementary Material

Refer to Web version on PubMed Central for supplementary material.

ACKNOWLEDGMENTS

Data Availability Statement

Data and scripts associated with this work are available at https://github.com/wines1/CrX3-QMC.

REFERENCES

(1). Huang B; Clark G; Navarro-Moratalla E; Klein DR; Cheng R; Seyler KL; Zhong D; Schmidgall E; McGuire MA; Cobden DH; Yao W; Xiao D; Jarillo-Herrero P; Xu X Layer-dependent ferromagnetism in a van der Waals crystal down to the monolayer limit. Nature 2017, 546, 270–273. [PubMed: 28593970]

(2). Bonilla M; Kolekar S; Ma Y; Diaz HC; Kalappattil V; Das R; Eggers T; Gutierrez HR; Phan M-H; Batzill M Strong room-temperature ferromagnetism in VSe2 monolayers on van der Waals substrates. Nat. Nanotechnol 2018, 13, 289–293. [PubMed: 29459653]

(3). Gong C; Li L; Li Z; Ji H; Stern A; Xia Y; Cao T; Bao W; Wang C; Wang Y; Qiu ZQ; Cava RJ; Louie SG; Xia J; Zhang X Discovery of intrinsic ferromagnetism in two-dimensional van der Waals crystals. Nature 2017, 546, 265–269. [PubMed: 28445468]

(4). Deng Y; Yu Y; Song Y; Zhang J; Wang NZ; Sun Z; Yi Y; Wu YZ; Wu S; Zhu J; Wang J; Chen XH; Zhang Y Gate-tunable room-temperature ferromagnetism in two-dimensional Fe3GeTe2. Nature 2018, 563, 94–99. [PubMed: 30349002]

(5). Torelli D; Moustafa H; Jacobsen KW; Olsen T High-throughput computational screening for two-dimensional magnetic materials based on experimental databases of three-dimensional compounds. npj Comp. Materials 2020, 6, 158.

(6). Dupont M; Kvashnin YO; Shiranzaei M; Fransson J; Laflorencie N; Kantian A Monolayer $CrCl_3$ as an Ideal Test Bed for the Universality Classes of 2D Magnetism. Phys. Rev. Lett 2021, 127, 037204. [PubMed: 34328783]

(7). Zhang W-B; Qu Q; Zhu P; Lam C-H Robust intrinsic ferromagnetism and half semiconductivity in stable two-dimensional single-layer chromium trihalides. J. Mater. Chem. C 2015, 3, 12457–12468.

(8). Kan M; Zhou J; Sun Q; Kawazoe Y; Jena P The Intrinsic Ferromagnetism in a MnO_2 Monolayer. J. Phys. Chem. Lett 2013, 4, 3382–3386. [PubMed: 26705581]

(9). Wines D; Saritas K; Ataca C Intrinsic Ferromagnetism of Two-Dimensional (2D) MnO_2 Revisited: A Many-Body Quantum Monte Carlo and DFT+U Study. J. Phys. Chem. C 2022, 126, 5813–5821.

(10). Saritas K; Ismail-Beigi S Piezoelectric ferromagnetism in two-dimensional materials via materials screening. Phys. Rev. B 2022, 106, 134421.

(11). Sachs B; Wehling TO; Novoselov KS; Lichtenstein AI; Katsnelson MI Ferromagnetic two-dimensional crystals: Single layers of K_2CuF_4. Phys. Rev. B 2013, 88, 201402.

(12). Chittari BL; Park Y; Lee D; Han M; MacDonald AH; Hwang E; Jung J Electronic and magnetic properties of single-layer MPX_3 metal phosphorous trichalcogenides. Phys. Rev. B 2016, 94, 184428.

(13). Sarikurt S; Kadioglu Y; Ersan F; Vatansever E; Akturk OU; Yuksel Y; Akinci U; Akturk E Electronic and magnetic properties of monolayer α-RuCl$_3$: a first-principles and Monte Carlo study. Phys. Chem. Chem. Phys 2018, 20, 997–1004. [PubMed: 29234762]

(14). Ersan F; Vatansever E; Sarikurt S; Yuksel Y; Kadioglu Y; Ozaydin HD; Akturk OU; Akinci U; Akturk E Exploring the electronic and magnetic properties of new metal halides from bulk to two-dimensional monolayer: RuX$_3$ (X = Br, I). J. Mag. Mag. Materials 2019, 476, 111–119.

(15). Foulkes WMC; Mitas L; Needs RJ; Rajagopal G Quantum Monte Carlo simulations of solids. Rev. Mod. Phys 2001, 73, 33–83.

(16). Hao H; Shee J; Upadhyay S; Ataca C; Jordan KD; Rubenstein BM Accurate Predictions of Electron Binding Energies of Dipole-Bound Anions via Quantum Monte Carlo Methods. J. Phys. Chem. Lett 2018, 9, 6185–6190. [PubMed: 30299101]

(17). Szyniszewski M; Mostaani E; Drummond ND; Fal'ko VI Binding energies of trions and biexcitons in two-dimensional semiconductors from Diffusion Quantum Monte Carlo calculations. Phys. Rev. B 2017, 95, 081301.

(18). Mostaani E; Szyniszewski M; Price CH; Maezono R; Danovich M; Hunt RJ; Drummond ND; Fal'ko VI Diffusion Quantum Monte Carlo study of excitonic complexes in two-dimensional transition-metal dichalcogenides. Phys. Rev. B 2017, 96, 075431.

(19). Saritas K; Krogel JT; Okamoto S; Lee HN; Reboredo FA Structural, electronic, and magnetic properties of bulk and epitaxial LaCoO$_3$ through Diffusion Monte Carlo. Phys. Rev. Materials 2019, 3, 124414.

(20). Luo Y; Benali A; Shulenburger L; Krogel JT; Heinonen O; Kent PRC Phase stability of TiO$_2$ polymorphs from Diffusion Quantum Monte Carlo. New J. Phys 2016, 18, 113049.

(21). Benali A; Shulenburger L; Krogel JT; Zhong X; Kent PRC; Heinonen O Quantum Monte Carlo analysis of a charge ordered insulating antiferromagnet: the Ti$_4$O$_7$ Magnéli phase. Phys. Chem. Chem. Phys 2016, 18, 18323–18335. [PubMed: 27334262]

(22). Santana JA; Krogel JT; Kim J; Kent PRC; Reboredo FA Structural stability and defect energetics of ZnO from Diffusion quantum Monte Carlo. J. Chem. Phys 2015, 142, 164705. [PubMed: 25933782]

(23). Saritas K; Krogel JT; Reboredo FA Relative energies and electronic structures of CoO polymorphs through ab initio Diffusion Quantum Monte Carlo. Phys. Rev. B 2018, 98, 155130.

(24). Wang G; Annaberdiyev A; Mitas L Binding and excitations in Si$_x$H$_y$ molecular systems using Quantum Monte Carlo. J. Chem. Phys 2020, 153, 144303. [PubMed: 33086844]

(25). Bennett MC; Hu G; Wang G; Heinonen O; Kent PRC; Krogel JT; Ganesh P Origin of metal-insulator transitions in correlated perovskite metals. Phys. Rev. Research 2022, 4, L022005.

(26). Annaberdiyev A; Wang G; Melton CA; Bennett MC; Mitas L Cohesion and excitations of diamond-structure silicon by quantum Monte Carlo: Benchmarks and control of systematic biases. Phys. Rev. B 2021, 103, 205206.

(27). Foyevtsova K; Krogel JT; Kim J; Kent PRC; Dagotto E; Reboredo FA Ab initio Quantum Monte Carlo Calculations of Spin Superexchange in Cuprates: The Benchmarking Case of Ca$_2$CuO$_3$. Phys. Rev. X 2014, 4, 031003.

(28). Busemeyer B; Dagrada M; Sorella S; Casula M; Wagner LK Competing collinear magnetic structures in superconducting FeSe by first-principles quantum Monte Carlo calculations. Phys. Rev. B 2016, 94, 035108.

(29). Saritas K; Krogel JT; Kent PRC; Reboredo FA Diffusion Monte Carlo: A pathway towards an accurate theoretical description of manganese oxides. Phys. Rev. Materials 2018, 2, 085801.

(30). Shin H; Krogel JT; Gasperich K; Kent PRC; Benali A; Heinonen O Optimized structure and electronic band gap of monolayer GeSe from Quantum Monte Carlo methods. Phys. Rev. Materials 2021, 5, 024002.

(31). Wines D; Saritas K; Ataca C A first-principles Quantum Monte Carlo study of two-dimensional (2D) GaSe. J. Chem. Phys 2020, 153, 154704. [PubMed: 33092365]

(32). Wines D; Saritas K; Ataca C A pathway toward high-throughput quantum Monte Carlo simulations for alloys: A case study of two-dimensional (2D) GaS_xSe_{1-x}. J. Chem. Phys 2021, 155, 194112. [PubMed: 34800964]

(33). Shulenburger L; Baczewski AD; Zhu Z; Guan J; Tománek D The Nature of the Interlayer Interaction in Bulk and Few-Layer Phosphorus. Nano Lett. 2015, 15, 8170–8175. [PubMed: 26523860]

(34). Frank T; Derian R; Tokár K; Mitas L; Fabian J; Štich I Many-Body Quantum Monte Carlo Study of 2D Materials: Cohesion and Band Gap in Single-Layer Phosphorene. Phys. Rev. X 2019, 9, 011018.

(35). Mostaani E; Drummond ND; Fal'ko VI Quantum Monte Carlo Calculation of the Binding Energy of Bilayer Graphene. Phys. Rev. Lett 2015, 115, 115501. [PubMed: 26406840]

(36). Kadioglu Y; Santana JA; Ozaydin HD; Ersan F; Akturk OU; Akturk E; Reboredo FA Diffusion Quantum Monte Carlo and density functional calculations of the structural stability of bilayer arsenene. J. Chem. Phys 2018, 148, 214706. [PubMed: 29884054]

(37). Saritas K; Ming W; Du M-H; Reboredo FA Excitation Energies of Localized Correlated Defects via Quantum Monte Carlo: A Case Study of Mn^{4+}-Doped Phosphors. J. Phys. Chem. Lett 2019, 10, 67–74. [PubMed: 30418779]

(38). Kylänpää I; Balachandran J; Ganesh P; Heinonen O; Kent PRC; Krogel JT Accuracy of ab initio electron correlation and electron densities in vanadium dioxide. Phys. Rev. Materials 2017, 1, 065408.

(39). Staros D; Hu G; Tiihonen J; Nanguneri R; Krogel J; Bennett MC; Heinonen O; Ganesh P; Rubenstein B A combined first principles study of the structural, magnetic, and phonon properties of monolayer CrI3. J. Chem. Phys 2022, 156, 014707. [PubMed: 34998345]

(40). Annaberdiyev A; Melton CA; Wang G; Mitas L Electronic structure of a-RuCl3 by fixed-node and fixed-phase diffusion Monte Carlo methods. Phys. Rev. B 2022, 106, 075127.

(41). Mermin ND; Wagner H Absence of Ferromagnetism or Antiferromagnetism in One- or Two-Dimensional Isotropic Heisenberg Models. Phys. Rev. Lett 1966, 17, 1133–1136.

(42). Torelli D; Olsen T Calculating critical temperatures for ferromagnetic order in two-dimensional materials. 2D Materials 2019, 6, 015028.

(43). Choudhary K; et al. The joint automated repository for various integrated simulations (JARVIS) for data-driven materials design. npj Comp. Materials 2020, 6, 173.

(44). Choudhary K; Cheon G; Reed E; Tavazza F Elastic properties of bulk and low-dimensional materials using van der Waals density functional. Phys. Rev. B 2018, 98, 014107.

(45). Choudhary K; Zhang Q; Reid ACE; Chowdhury S; Van Nguyen N; Trautt Z; Newrock MW; Congo FY; Tavazza F Computational screening of high-performance optoelectronic materials using OptB88vdW and TB-mBJ formalisms. Scientific Data 2018, 5, 180082. [PubMed: 29737975]

(46). Choudhary K; Garrity KF; Tavazza F Data-driven discovery of 3D and 2D thermoelectric materials. J. Phys. Cond. Matter 2020, 32, 475501.

(47). Choudhary K; Garrity KF; Sharma V; Biacchi AJ; Hight Walker AR; Tavazza F High-throughput density functional perturbation theory and machine learning predictions of infrared, piezoelectric, and dielectric responses. npj Comp Materials 2020, 6, 64.

(48). Choudhary K; Bercx M; Jiang J; Pachter R; Lamoen D; Tavazza F Accelerated Discovery of Efficient Solar Cell Materials Using Quantum and Machine-Learning Methods. Chem. Mater 2019, 31, 5900–5908.

(49). Choudhary K; Garrity KF; Jiang J; Pachter R; Tavazza F Computational search for magnetic and non-magnetic 2D topological materials using unified spin-orbit spillage screening. npj Comp. Materials 2020, 6, 49.

(50). Choudhary K; Tavazza F Predicting anomalous quantum confinement effect in van der Waals materials. Phys. Rev. Materials 2021, 5, 054602.

(51). Choudhary K; Garrity K Designing high-TC superconductors with BCS-inspired screening, density functional theory, and deep-learning. npj Comp. Materials 2022, 8, 244.

(52). Himmetoglu B; Floris A; de Gironcoli S; Cococcioni M Hubbard-corrected DFT energy functionals: The LDA+U description of correlated systems. Int. J. Quantum Chem 2014, 114, 14–49.

(53). Sun J; Ruzsinszky A; Perdew JP Strongly Constrained and Appropriately Normed Semilocal Density Functional. Phys. Rev. Lett 2015, 115, 036402. [PubMed: 26230809]

(54). Furness JW; Kaplan AD; Ning J; Perdew JP; Sun J Accurate and Numerically Efficient r2SCAN Meta-Generalized Gradient Approximation. J. Phys. Chem. Lett 2020, 11, 8208–8215. [PubMed: 32876454]

(55). Heyd J; Scuseria GE; Ernzerhof M Hybrid functionals based on a screened Coulomb potential. J. Chem. Phys 2003, 118, 8207–8215.

(56). Dudarev SL; Botton GA; Savrasov SY; Humphreys CJ; Sutton AP Electron-energy-loss spectra and the structural stability of nickel oxide: An LSDA+U study. Phys. Rev. B 1998, 57, 1505–1509.

(57). Zhang Z; Shang J; Jiang C; Rasmita A; Gao W; Yu T Direct Photoluminescence Probing of Ferromagnetism in Monolayer Two-Dimensional CrBr3. Nano Lett. 2019, 19, 3138–3142. [PubMed: 30945874]

(58). Cai X; Song T; Wilson NP; Clark G; He M; Zhang X; Taniguchi T; Watanabe K; Yao W; Xiao D; McGuire MA; Cobden DH; Xu X Atomically Thin CrCl3: An In-Plane Layered Antiferromagnetic Insulator. Nano Lett. 2019, 19, 3993–3998. [PubMed: 31083954]

(59). Kresse G; Furthmüller J Efficient iterative schemes for ab initio total-energy calculations using a plane-wave basis set. Phys. Rev. B 1996, 54, 11169–11186.

(60). Kresse G; Joubert D From ultrasoft pseudopotentials to the projector augmented-wave method. Phys. Rev. B 1999, 59, 1758–1775.

(61). Perdew JP; Burke K; Ernzerhof M Generalized Gradient Approximation Made Simple. Phys. Rev. Lett 1996, 77, 3865–3868. [PubMed: 10062328]

(62). Hohenberg P; Kohn W Inhomogeneous Electron Gas. Phys. Rev 1964, 136, B864–B871.

(63). Klimeš J; Bowler DR; Michaelides A Chemical accuracy for the van der Waals density functional. J. Phys. Cond. Matter 2010, 22, 022201.

(64). Giannozzi P; et al. QUANTUM ESPRESSO: a modular and open-source software project for quantum simulations of materials. J. Phys.: Cond. Matter 2009, 21, 395502.

(65). Krogel JT; Santana JA; Reboredo FA Pseudopotentials for quantum Monte Carlo studies of transition metal oxides. Phys. Rev. B 2016, 93, 075143.

(66). Bennett MC; Wang G; Annaberdiyev A; Melton CA; Shulenburger L; Mitas L A new generation of effective core potentials from correlated calculations: 2nd row elements. J. Chem. Phys 2018, 149, 104108. [PubMed: 30219005]

(67). Wang G; Annaberdiyev A; Melton CA; Bennett MC; Shulenburger L; Mitas L A new generation of effective core potentials from correlated calculations: 4s and 4p main group elements and first row additions. J. Chem. Phys 2019, 151, 144110. [PubMed: 31615226]

(68). Wang G; Kincaid B; Zhou H; Annaberdiyev A; Bennett MC; Krogel JT; Mitas L A new generation of effective core potentials from correlated and spin-orbit calculations: Selected heavy elements. J. Chem. Phys 2022, 157, 054101. [PubMed: 35933201]

(69). Kim J; et al. QMCPACK: an open source ab initio quantum Monte Carlo package for the electronic structure of atoms, molecules and solids. J. Phys.: Cond. Matter 2018, 30, 195901.

(70). Kent PRC; et al. QMCPACK: Advances in the development, efficiency, and application of auxiliary field and real-space Variational and Diffusion Quantum Monte Carlo. J. Chem. Phys 2020, 152, 174105. [PubMed: 32384844]

(71). Needs RJ; Towler MD; Drummond ND; López Ríos P Continuum Variational and Diffusion Quantum Monte Carlo calculations. J. Phys. Cond. Matter 2010, 22, 023201.

(72). Slater JC The Theory of Complex Spectra. Phys. Rev 1929, 34, 1293–1322.

(73). Jastrow R Many-Body Problem with Strong Forces. Phys. Rev 1955, 98, 1479–1484.

(74). Umrigar CJ; Filippi C Energy and Variance Optimization of Many-Body Wave Functions. Phys. Rev. Lett 2005, 94, 150201. [PubMed: 15904123]

(75). Mitas L; Shirley EL; Ceperley DM Nonlocal pseudopotentials and Diffusion Monte Carlo. J. Chem. Phys 1991, 95, 3467–3475.

(76). Drummond ND; Towler MD; Needs RJ Jastrow correlation factor for atoms, molecules, and solids. Phys. Rev. B 2004, 70, 235119.

(77). Umrigar CJ; Toulouse J; Filippi C; Sorella S; Hennig RG Alleviation of the Fermion-Sign Problem by Optimization of Many-Body Wave Functions. Phys. Rev. Lett 2007, 98, 110201. [PubMed: 17501026]

(78). Krogel JT Nexus: A modular workflow management system for quantum simulation codes. Comput. Phys. Commun 2016, 198, 154–168.

(79). Casula M; Moroni S; Sorella S; Filippi C Size-consistent variational approaches to nonlocal pseudopotentials: Standard and lattice regularized diffusion Monte Carlo methods revisited. J. Chem. Phys 2010, 132, 154113. [PubMed: 20423174]

(80). Lado JL; Fernández-Rossier J On the origin of magnetic anisotropy in two dimensional CrI_3. 2D Materials 2017, 4, 035002.

(81). Xu C; Feng J; Prokhorenko S; Nahas Y; Xiang H; Bellaiche L Topological spin texture in Janus monolayers of the chromium trihalides $Cr(I, X)_3$. Phys. Rev. B 2020, 101, 060404.

(82). Xu C; Feng J; Xiang H; Bellaiche L Interplay between Kitaev interaction and single ion anisotropy in ferromagnetic CrI3 and CrGeTe3 monolayers. npj Comp. Materials 2018, 4, 57.

(83). Lee I; Utermohlen FG; Weber D; Hwang K; Zhang C; van Tol J; Goldberger JE; Trivedi N; Hammel PC Fundamental Spin Interactions Underlying the Magnetic Anisotropy in the Kitaev Ferromagnet CrI_3. Phys. Rev. Lett 2020, 124, 017201. [PubMed: 31976706]

(84). Choudhary K; Tavazza F Convergence and machine learning predictions of Monkhorst-Pack k-points and plane-wave cut-off in high-throughput DFT calculations. Comput. Mater. Sci 2019, 161, 300–308.

(85). Mejía-Rodríguez D; Trickey SB Analysis of overmagnetization of elemental transition metal solids from the SCAN density functional. Phys. Rev. B 2019, 100, 041113.

(86). Fu Y; Singh DJ Density functional methods for the magnetism of transition metals: SCAN in relation to other functionals. Phys. Rev. B 2019, 100, 045126.

(87). Kitchaev DA; Peng H; Liu Y; Sun J; Perdew JP; Ceder G Energetics of MnO_2 polymorphs in density functional theory. Phys. Rev. B 2016, 93, 045132.

(88). Morosin B; Narath A X-Ray Diffraction and Nuclear Quadrupole Resonance Studies of Chromium Trichloride. J. Chem. Phys 1964, 40, 1958–1967.

(89). Olsen T Unified Treatment of Magnons and Excitons in Monolayer CrI_3 from Many-Body Perturbation Theory. Phys. Rev. Lett 2021, 127, 166402. [PubMed: 34723581]

(90). Kumar Gudelli V; Guo G-Y Magnetism and magneto-optical effects in bulk and few-layer CrI3: a theoretical GGA+U study. New J. Phys 2019, 21, 053012.

(91). Webster L; Yan J-A Strain-tunable magnetic anisotropy in monolayer $CrCl_3$, $CrBr_3$, and CrI_3. Phys. Rev. B 2018, 98, 144411.

(92). Pizzochero M; Yadav R; Yazyev OV Magnetic exchange interactions in monolayer CrI_3 from many-body wavefunction calculations. 2D Materials 2020, 7, 035005.

(93). Kwon Y; Ceperley DM; Martin RM Effects of three-body and backflow correlations in the two-dimensional electron gas. Phys. Rev. B 1993, 48, 12037–12046.

(94). Kwon Y; Ceperley DM; Martin RM Effects of backflow correlation in the three-dimensional electron gas: Quantum Monte Carlo study. Phys. Rev. B 1998, 58, 6800–6806.

(95). López Ríos P; Ma A; Drummond ND; Towler MD; Needs RJ Inhomogeneous backflow transformations in quantum Monte Carlo calculations. Phys. Rev. E 2006, 74, 066701.

(96). Bajdich M; Tiago ML; Hood RQ; Kent PRC; Reboredo FA Systematic Reduction of Sign Errors in Many-Body Calculations of Atoms and Molecules. Phys. Rev. Lett 2010, 104, 193001. [PubMed: 20866961]

(97). Ichibha T; Dzubak AL; Krogel JT; Cooper VR; Reboredo FA CrI_3 revisited with a many-body ab initio theoretical approach. Phys. Rev. Materials 2021, 5, 064006.
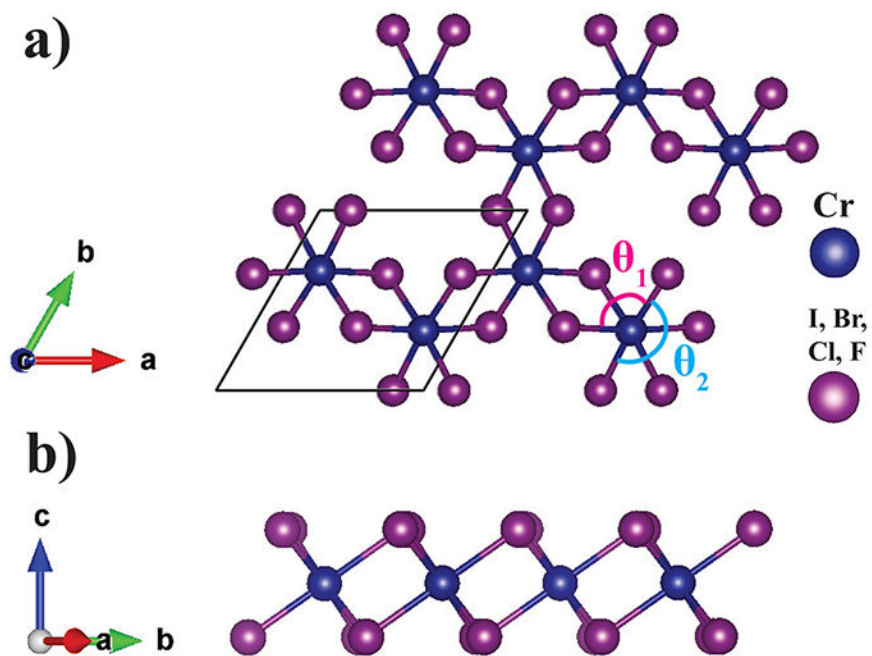
Figure 1.
Top (a) and side (b) views of the atomic structure of monolayer CrX_3 (X = I, Br, Cl, F). More detailed structural parameters are given in Table S2.
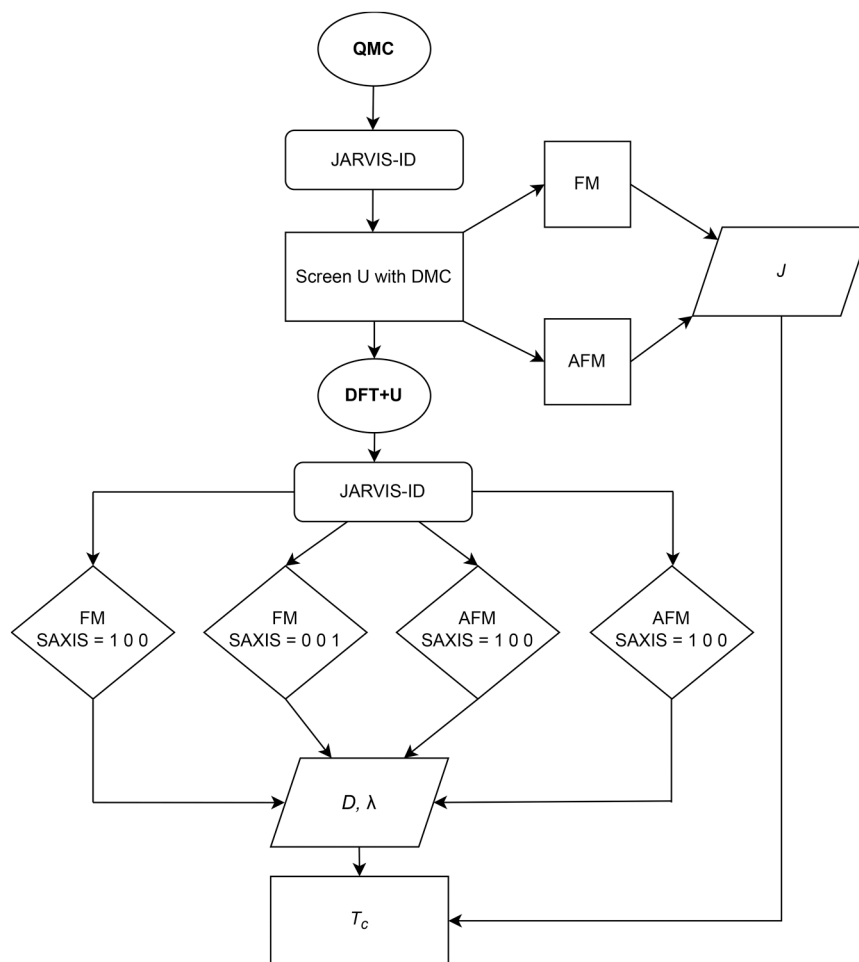
Figure 2.
Full high-throughput workflow proposed in this work to obtain the accurate magnetic properties of a 2D system using a combination of DFT+U and QMC.
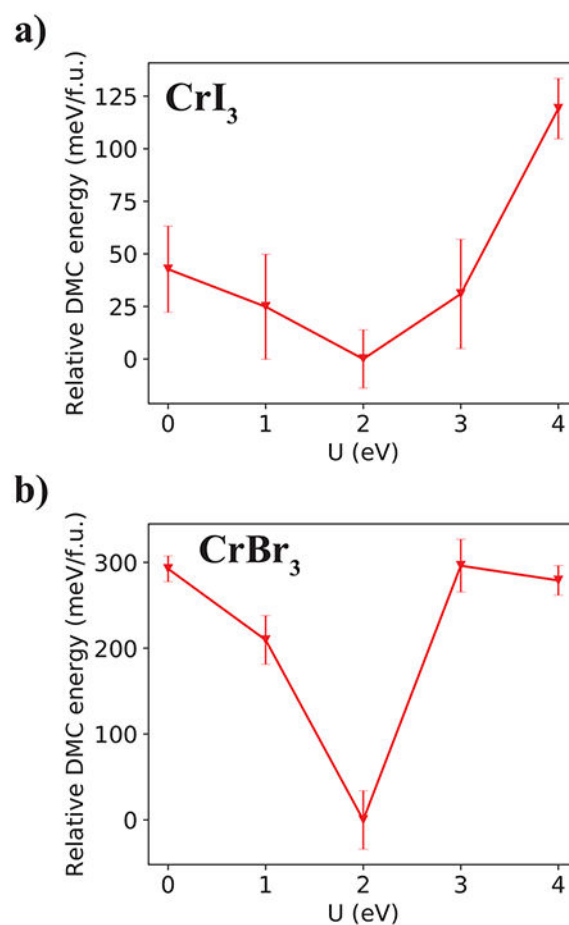
Figure 3.
DMC-calculated total energies and subsequent standard error about the mean (indicated by error bars) of a 16 atom supercell (normalized per formula unit (f.u.)) of the ferromagnetic orientation of 2D (a) CrI_3 and (b) $CrBr_3$ calculated as a function of the U parameter used to variationally determine the optimal trial wave function. For convenience of presentation, the DMC energies are shifted by the lowest DMC energy obtained at the appropriate U value (U = 2 eV for CrI_3 and $CrBr_3$).
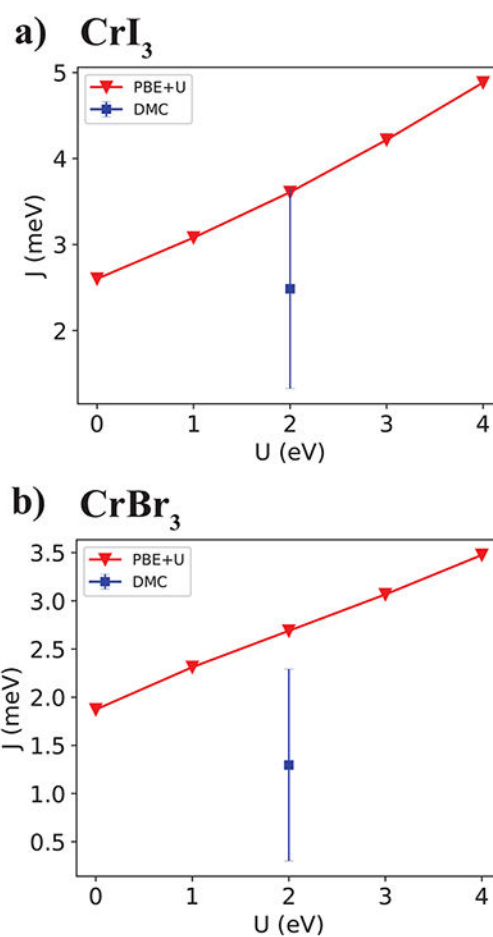
Figure 4.
Values of J for 2D (a) CrI_3 and (b) $CrBr_3$ as a function of U calculated with PBE+U (red) and DMC (blue, using PBE+2 to create the trial wavefuction). Both methods used NC pseudopotentials in the calculation, and a 48 atom supercell was used for each material. The standard error about the mean is indicated by error bars for DMC in blue.
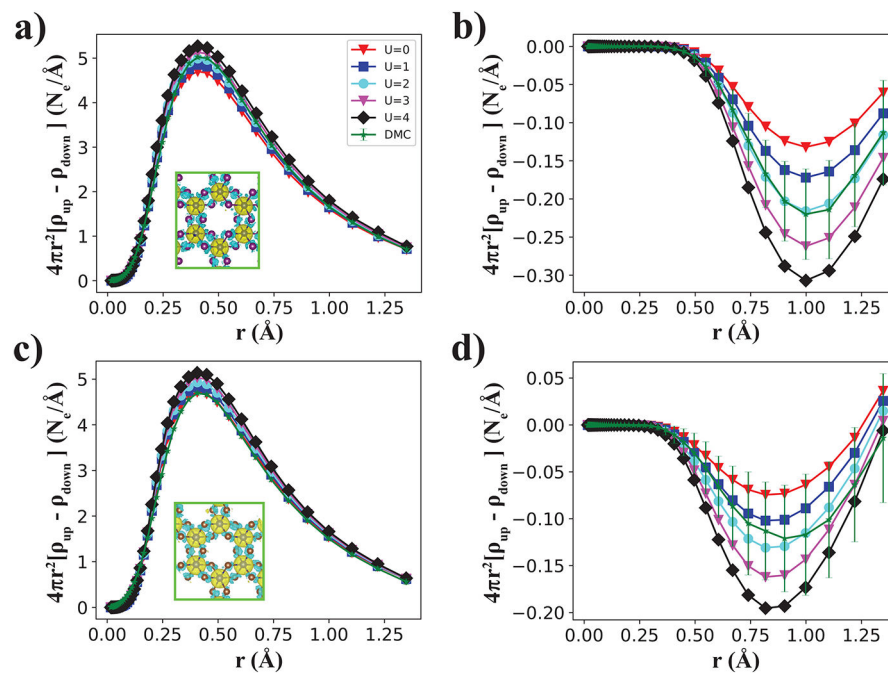
Figure 5.
Radially averaged spin density ($\rho_{\text{up}} - \rho_{\text{down}}$) as a function of distance, calculated with DMC and PBE+U (U = [0, 1, 2, 3, 4] eV) of (a) Cr and (b) I for 2D CrI$_3$ and (c) Cr and (d) Br for 2D CrBr$_3$. The insets of (a) and (c) depict the spin isosurface density of CrI$_3$ and CrBr$_3$ respectively, where the isosurface value was set to 5×10^{-5} e/Å^3. The standard error about the mean for DMC is indicated by error bars in green.

Table 1.

Benchmarking Noncollinear DFT and DFT+U ($U = 2$ eV) Data Calculated with Various Functionals (PBE, LDA, SCAN, r2SCAN, HSE06) and the VASP Code with PAW Pseudopotentials for CrX_3 Monolayers[a]

CrI_3 Functional	J (meV)	D (meV)	λ (meV)	T_c (K)
PBE	2.83	0.192	0.173	38.33
PBE+U	3.70	0.075	0.161	43.60
LDA	1.98	0.139	0.126	27.09
LDA+U	2.80	0.054	0.147	34.21
SCAN	3.24	−0.129	0.019	-
SCAN+U	4.06	−0.069	0.216	46.23
r2SCAN	2.57	0.145	0.049	29.00
r2SCAN+U	3.08	0.146	0.044	32.91
HSE06	4.22	0.068	0.173	48.63

$CrBr_3$ Functional	J (meV)	D (meV)	λ (meV)	T_c (K)
PBE	2.14	0.035	0.032	20.36
PBE+U	2.85	0.020	0.032	24.28
LDA	1.44	0.041	0.031	15.23
LDA+U	2.45	0.025	0.031	21.82
SCAN	1.63	0.083	−0.016	13.40
SCAN+U	1.83	0.016	−0.052	-
r2SCAN	1.85	0.037	0.013	16.21
r2SCAN+U	1.98	0.024	0.016	16.68
HSE06	2.16	0.011	0.014	16.17

$CrCl_3$ Functional	J (meV)	D (meV)	λ (meV)	T_c (K)
PBE	1.20	0.002	0.007	8.44
PBE+U	2.04	−0.003	0.009	12.44
LDA	0.49	0.011	0.002	4.14
LDA+U	1.87	0.009	0.002	10.69
SCAN	0.94	0.032	−0.003	7.64
SCAN+U	1.33	0.005	0.004	8.57
r2SCAN	1.42	0.007	0.004	9.33
r2SCAN+U	1.80	0.007	0.004	11.26
HSE06	1.89	0.006	0.000	8.91

CrF_3 Functional	J (meV)	D (meV)	λ (meV)	Tc (K)
PBE	1.53	0.055	0.000	13.45
PBE+U	1.33	0.053	−0.001	11.91
LDA	1.87	0.068	0.003	16.83
LDA+U	1.63	0.065	0.002	14.91
SCAN	1.41	−0.028	−0.044	-

SCAN+U	1.29	0.048	−0.013	8.97
r2SCAN	1.66	0.023	0.000	11.38
r2SCAN+U	1.44	0.050	−0.002	12.22
HSE06	1.02	0.053	−0.001	9.79

[a]Values for J, D, λ, and T_C are given for each functional and material. It is important to note that the geometry in these calculations is fixed to the geometry obtained from the JARVIS-2D DFT database (relaxed with vdW-DF-OptB88).

Table 2.

Benchmarking Noncollinear DFT and DFT+U ($U = 2$ eV) Data Calculated with Various Functionals (PBE, LDA, SCAN, r2SCAN, HSE06) and the VASP Code with PAW Pseudopotentials for CrX$_3$ Monolayers[a]

CrI$_3$ Functional	J (meV)	D (meV)	λ (meV)	T_c (K)
PBE	2.80	0.211	0.176	38.42
PBE+U	3.84	0.077	0.182	46.06
LDA	1.13	0.149	0.117	17.61
LDA+U	2.54	0.083	0.148	32.52
SCAN	2.73	0.041	0.071	28.61
SCAN+U	4.00	−0.089	0.167	41.69
r2SCAN	2.58	0.142	0.057	29.48
r2SCAN+U	3.17	0.345	−0.077	30.72
CrBr$_3$ Functional	J (meV)	D (meV)	λ (meV)	T_c (K)
PBE	2.48	0.041	0.036	23.53
PBE+U	3.12	0.016	0.044	27.52
LDA	0.13	0.040	0.028	2.51
LDA+U	2.01	0.022	0.028	18.37
SCAN	1.73	0.050	0.018	16.64
SCAN+U	1.89	0.061	0.011	17.56
r2SCAN	1.95	0.037	0.020	17.76
r2SCAN+U	2.01	0.023	0.020	17.29
CrCl$_3$ Functional	J (meV)	D (meV)	λ (meV)	T_c (K)
PBE	1.78	−0.022	0.026	13.49
PBE+U	2.41	−0.029	0.028	16.77
LDA	−1.46	0.009	0.002	-
LDA+U	1.26	0.006	0.001	7.48
SCAN	1.04	0.041	0.012	10.64
SCAN+U	1.26	0.032	−0.023	-
r2SCAN	1.57	−0.012	0.024	12.67
r2SCAN+U	1.92	−0.018	0.026	14.63
CrF$_3$ Functional	J (meV)	D (meV)	λ (meV)	T_c (K)
PBE	1.74	0.058	0.001	15.12
PBE+U	1.44	0.057	−0.001	12.86
LDA	1.12	0.067	0.003	11.41
LDA+U	1.55	0.061	−0.001	13.86
SCAN	1.49	0.025	−0.007	8.52
SCAN+U	1.22	0.044	−0.006	9.76
r2SCAN	1.68	0.037	0.008	14.38
r2SCAN+U	1.42	0.049	0.020	14.45

[a]Values for J, D, λ, and T_C are given for each functional and material. For these calculations, the geometry was relaxed using each respective functional, using collinear spin-polarized DFT for the FM orientation of each material. After this preliminary relaxation, the geometry was fixed and used in the DFT workflow to calculate T_C.

Table 3.

Calculated J with PBE+U and DMC (Both Using NC Pseudopotentials) and the Ising Temperature (T_c^{Ising}) and Curie Temperatures (T_c) Calculated with the Torelli and Olsen Model[a]

CrI$_3$ Method	J (meV)	T_c^{Ising} (K)	$T_c^{\text{PBE}+2}$ (K)	$T_c^{\text{LDA}+2}$ (K)	$T_c^{\text{SCAN}+2}$ (K)	$T_c^{\text{r2SCAN}+2}$ (K)	T_c^{HSE06} (K)
PBE+0	2.60	103.26	33.46	32.40	33.10	29.00	33.81
PBE+1	3.08	122.23	37.98	36.78	37.57	32.91	38.38
PBE+2	3.61	143.23	42.79	41.42	42.32	37.07	43.23
PBE+3	4.22	167.39	48.10	46.57	47.58	41.67	48.60
PBE+4	4.88	193.84	53.70	51.99	53.12	46.52	54.26
DMC	2.49(1.16)	98.65(46.02)	32.34(10.78)	31.31(10.43)	31.98(10.66)	28.02(9.33)	32.67(10.89)

CrBr$_3$ Method	J (meV)	T_c^{Ising} (K)	$T_c^{\text{PBE}+2}$ (K)	$T_c^{\text{LDA}+2}$ (K)	$T_c^{\text{SCAN}+2}$ (K)	$T_c^{\text{r2SCAN}+2}$ (K)	T_c^{HSE06} (K)
PBE+0	1.87	74.31	17.70	17.84	-	15.98	14.52
PBE+1	2.31	91.76	20.74	20.90	-	18.72	17.01
PBE+2	2.69	106.74	23.23	23.41	-	20.97	19.05
PBE+3	3.07	121.72	25.63	25.84	-	23.14	21.03
PBE+4	3.48	137.97	28.16	28.38	-	25.42	23.10
DMC	1.30(1.00)	51.45(39.52)	13.43(7.17)	13.54(7.23)	-	12.13(6.47)	11.02(5.88)

[a]Columns 4–8 use various functionals for the MA from the VASP (PAW) calculations from the DFT Benchmarking section (at $U = 2$ eV) indicated by the superscript on T_c. The associated uncertainty of the DMC quantities are given in parentheses.

Table 4.

Site-Averaged Atomic Magnetic Moments (in μ_B) of Cr and I for 2D CrI_3 and Cr and Br for 2D $CrBr_3$, Estimated by Integrating the Spin Density for DMC and PBE+U Results[a]

CrI_3 Method	M_{Cr} (μ_B)	M_I (μ_B)
PBE+0	3.06	−0.08
PBE+1	3.15	−0.1
PBE+2	3.25	−0.13
PBE+3	3.34	−0.16
PBE+4	3.43	−0.18
DMC	3.21(5)	−0.13(5)
$CrBr_3$ Method	M_{Cr} (μ_B)	M_{Br} (μ_B)
PBE+0	3.01	−0.03
PBE+1	3.07	−0.05
PBE+2	3.14	−0.07
PBE+3	3.2	−0.09
PBE+4	3.26	−0.11
DMC	2.96(5)	−0.07(5)

[a] DMC uncertainties are given in the parentheses.